

# Cracking the dark matter code at the LHC

Won Sang Cho,<sup>1</sup> Doojin Kim,<sup>2</sup> Konstantin T. Matchev,<sup>1</sup> and Myeonghun Park<sup>3</sup>

<sup>1</sup>*Physics Department, University of Florida, Gainesville, FL 32611, USA*

<sup>2</sup>*Department of Physics, University of Maryland, College Park, MD 20742, USA*

<sup>3</sup>*CERN, Theory Division, CH-1211 Geneva 23, Switzerland*

(Dated: June 7, 2012)

We consider the decay of a generic resonance to two visible particles and any number of invisible particles. We show that the shape of the invariant mass distribution of the two visible particles is sensitive to both the mass spectrum of the new particles, as well as the decay topology. We provide the analytical formulas describing the invariant mass shapes for the nine simplest topologies (with up to two invisible particles in the final state). Any such distribution can be simply categorized by its endpoint, peak location and curvature, which are typically sufficient to discriminate among the competing topologies. In each case, we list the effective mass parameters which can be measured by experiment. In certain cases, the invariant mass shape is sufficient to completely determine the new particle mass spectrum, including the overall mass scale.

PACS numbers: 14.80.Ly, 12.60.Jv, 13.85.-t

The dark matter problem and the mystery of the feeble neutrinos greatly motivate the ongoing LHC searches for new physics in channels with missing energy. Alas, at hadron colliders like the LHC, deciphering events with invisible particles in the final state is notoriously difficult.

The problem is schematically illustrated in Fig. 1, which depicts the generic decay of some new heavy resonance  $A$  into  $N_v$  visible particles  $v_i$  and  $N_\chi$  “invisible” particles  $\chi_i$  (neutrinos or dark matter candidates) which leave no trace in the detector. A priori we have no way of knowing the underlying physics behind Fig. 1, and thus we are missing the answers to some very basic questions: 1) How many invisible particles are in the final state? 2) What are their masses? 3) What is the exact topology (i.e. Feynman diagram) of Fig. 1: are there any intermediate resonances, and if so, what are their masses?

Historically, the topic of mass measurements has attracted the most attention in the literature (for a review, see [1]). Unfortunately, virtually all proposed methods suffer from two drawbacks. First, one must typically assume the correct decay topology for Fig. 1, *including* the correct number  $N_\chi$  of invisible particles. If this guess is incorrect, the method does not apply. This motivates us to address the issue of the correct decay topology and number of invisibles concurrently with (perhaps even prior to) the more traditional question of mass measurements [2]. Second, most methods for mass measurements utilize kinematic endpoints, where the available statistics can be rather poor (in the sense that the most populated bins are rarely near the kinematic endpoint). Here we shall instead concentrate on the region near the *peak* rather than the endpoint of the kinematic distribution. (The exact shape *in the vicinity* of the endpoint does contain information about  $N_\chi$  [3, 4], but is difficult to measure precisely in the presence of backgrounds and detector effects.) Our main result will be the derivation of the analytical formulas necessary to analyze the full shape of the invariant mass distributions of the visible particles in Fig. 1, including the location of the peak. We shall then

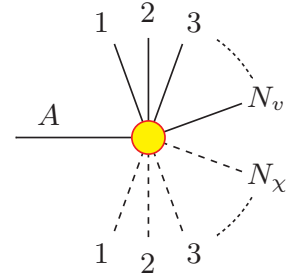


FIG. 1: The generic decay topology under consideration.

TABLE I: The number of inequivalent event topologies as a function of  $1 \leq N_v \leq 4$  and  $1 \leq N_\chi \leq 5$ .

$N_v$	$N_\chi$				
	1	2	3	4	5
1	1	2	4	8	16
2	2	7	20	55	142
3	4	20	78	270	860
4	8	55	270	1138	4294

demonstrate how those results can be used to determine: 1) the number of missing particles; 2) their masses; and 3) the associated event topology.

Our setup is as follows. We consider the generic decay from Fig. 1 without any prior assumptions about the decay topology or the number of invisibles. As seen in Table I, the number of inequivalent decay topologies proliferates very quickly as we increase the number of particles in the final state. Let us begin with the simplest and most challenging case of  $N_v = 2$ , postponing  $N_v > 2$  to a future study [5]. According to Table I, there are 2 topologies with  $N_\chi = 1$ , shown in Fig. 2(a,b), and 7 topologies with  $N_\chi = 2$ , shown in Fig. 2(c-i). Our main goal is to analyze and contrast the  $v_1 v_2$  invariant mass

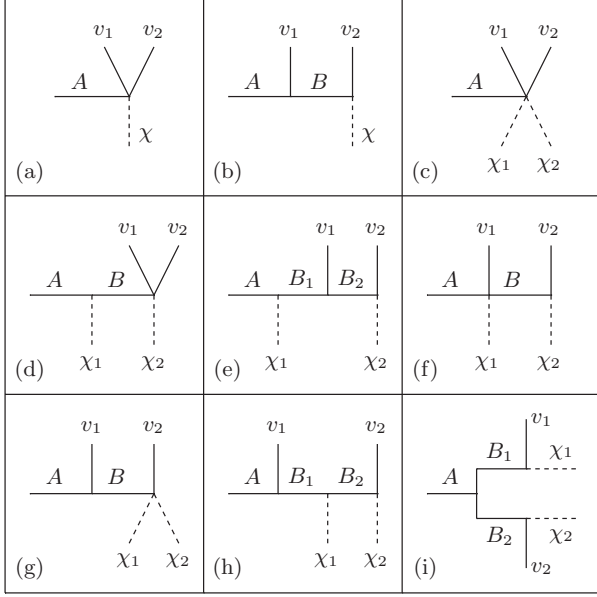


FIG. 2: The nine  $N_v = 2$  topologies with  $N_\chi \leq 2$ .

distribution<sup>1</sup> in each of those nine cases.

The differential distribution of the invariant mass  $m \equiv m_{v_1 v_2}$  will be described by an analytical formula

$$\frac{dN}{dm} \equiv f(m; M_A, M_{B_i}, M_{\chi_j}), \quad (1)$$

which is a function of the unknown masses. Given the general formula (1) for  $f(m)$ , we can easily obtain its kinematic endpoint

$$E \equiv \max \{m\} \quad (2)$$

and the location  $P$  of the peak of the  $f(m)$  distribution

$$f(m = P) \equiv \max \{f(m)\}. \quad (3)$$

Let us also define the dimensionless derivative ratios

$$R_n \equiv - \left( \frac{m^n}{f(m)} \frac{d^n f(m)}{dm^n} \right)_{m=P}. \quad (4)$$

By definition,  $R_1 = 0$ , as long as  $f(m)$  is continuously differentiable at  $m = P$ , while  $R_2$  parameterizes the curvature of  $f(m)$  at  $m = P$ .

The parameters  $E$ ,  $P$  and  $R_n$  are in principle all experimentally measurable from the distribution (1). Traditional studies [7] have always concentrated on measuring

just the endpoint  $E$ , failing to utilize all of the available information encoded in the distribution  $f(m)$ . The endpoint approach gives a single measurement (2), which is clearly insufficient to determine the full spectrum of resonances involved in the decay chain of Fig. 1. Here we propose to invoke the full shape (1) in the analysis. We envision that in practice this will be done by performing unbinned maximum-likelihood fits of (1) to the observed data. In order to illustrate the power of the method here, it is sufficient to consider just the additional individual measurements of  $P$  and  $R_2$ . Since they are obtained from the most populated bins near the peak, we can expect that they will be rather well measured. More importantly, the additional information about  $P$  and  $R_2$  might be sufficient to completely determine the mass spectrum (see eqs. (13,14) below). But first we need to present our results for (1-4) in each of the nine cases in Fig. 2.

*The topology of Fig. 2(a).* For a three body decay to massless visible particles, one has

$$f(m; M_A, M_\chi) \sim m \lambda^{1/2} (m^2, M_A^2, M_\chi^2), \quad (5)$$

where

$$\lambda(x, y, z) \equiv x^2 + y^2 + z^2 - 2xy - 2yz - 2xz. \quad (6)$$

In this case

$$E = M_A - M_\chi, \quad (7)$$

$$P = \left[ 2M_A M_\chi \left( 2 - \sqrt{1 + 3\alpha^2} \right) / (3\alpha) \right]^{1/2}, \quad (8)$$

$$R_2 = 6 \left[ 1 + (1 + 3\alpha^2)^{-1/2} \right]^{-1}, \quad (9)$$

where

$$\alpha \equiv 2M_A M_\chi / (M_A^2 + M_\chi^2). \quad (10)$$

Contrary to popular belief, one can now solve for both masses  $M_A$  and  $M_\chi$ , given two of the three measurements (7-9). For example, using the peak location  $P$  and the endpoint  $E$ , we find

$$M_A = \frac{E}{2} \left( \frac{P}{E} \sqrt{\frac{2 - 3(P/E)^2}{1 - 2(P/E)^2}} + 1 \right), \quad (11)$$

$$M_\chi = \frac{E}{2} \left( \frac{P}{E} \sqrt{\frac{2 - 3(P/E)^2}{1 - 2(P/E)^2}} - 1 \right). \quad (12)$$

Eqs. (11,12) offer a new method of determining *both*  $M_A$  and  $M_\chi$ , which is a simpler alternative to the  $M_{T2}$  kink method of [8], since here we do not rely on the  $\cancel{E}_T$  measurement at all, and do not require to reconstruct the decay chain on the other side of the event.

In fact, one does not even need an endpoint measurement, since the peak location  $P$  and the curvature  $R_2$  are sufficient for this purpose:

$$M_A = \frac{P}{\sqrt{2}} \left( \frac{6 - R_2}{4 - R_2} + \sqrt{\frac{12 - R_2}{4 - R_2}} \right)^{1/2}, \quad (13)$$

<sup>1</sup> We note that the resonance  $A$  is in general allowed to be produced fully inclusively, with an arbitrary number of *additional* visible or invisible particles recoiling against  $A$  in the event. This precludes us from using the  $\cancel{E}_T$  measurement, since it will be corrupted by the invisible recoils, which leaves us with  $m_{v_1 v_2}$  as the only viable observable to study. The related combinatorial problem of partitioning the visibles in the event was addressed in [2, 6].

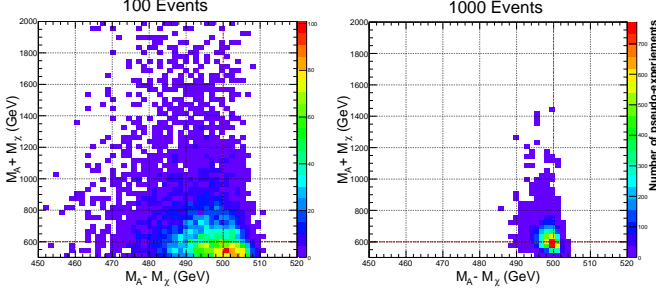


FIG. 3: Distribution of  $M_A$  and  $M_\chi$  found by a maximum-likelihood fit to eq. (5) in 10,000 pseudo-experiments with 100 signal events (left) or 1000 signal events (right). The input study point has  $M_A = 550$  GeV and  $M_\chi = 50$  GeV.

$$M_\chi = \frac{P}{\sqrt{2}} \left( \frac{6 - R_2}{4 - R_2} - \sqrt{\frac{12 - R_2}{4 - R_2}} \right)^{1/2}. \quad (14)$$

To the best of our knowledge (13,14) represent the first and only method in the literature which is capable of determining the complete mass spectrum in a short SUSY-like decay chain, without relying on any kinematic end-point measurements.

In order to get a rough idea of the precision of these mass determinations, in Fig. 3 on the left (right) we show the results from 10,000 pseudo-experiments with 100 (1000) signal events each. In each pseudo-experiment, the two masses  $M_A$  and  $M_\chi$  are extracted from a maximum-likelihood fit of the simulated data to the full distribution (5). Fig. 3 shows that, as expected, the mass difference is measured quite well, at the level of  $\sim 1\%$  with just 100 events. At the same time, the mass sum (or equivalently, the absolute mass scale) is also being determined, albeit less precisely: at the level of  $\sim 30\%$  ( $\sim 10\%$ ) with 100 (1000) events.

*The topology of Fig. 2(b).* Here one obtains the celebrated triangular shape

$$f(m) \sim m, \quad (15)$$

$$E = P = \sqrt{(M_A^2 - M_B^2)(1 - M_\chi^2/M_B^2)}, \quad (16)$$

$$R_2 = \infty. \quad (17)$$

Unfortunately, the masses enter the shape (15) only through the combination (16), which is the single effective mass parameter accessible experimentally.

*The topology of Fig. 2(c).* The shape is more conveniently given in integral form, which is easy to code up:

$$f(m) \sim m \int_{(M_{\chi_1} + M_{\chi_2})^2}^{(M_A - m)^2} \frac{ds}{s} \sqrt{\lambda(M_A^2, m^2, s) \lambda(s, M_{\chi_1}^2, M_{\chi_2}^2)}, \quad (18)$$

$$E = M_A - M_{\chi_1} - M_{\chi_2}. \quad (19)$$

The explicit formulas for  $P$  and (18) will be shown in [5]. The important point is that in principle all three masses

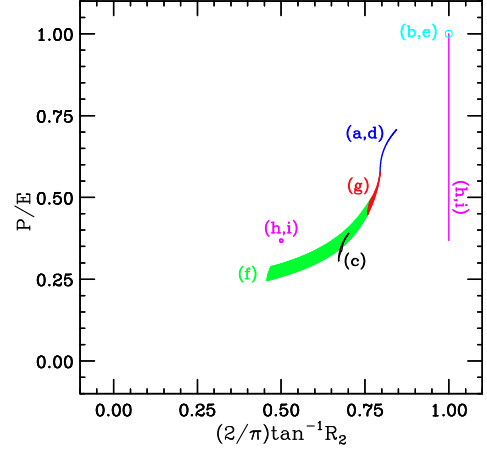


FIG. 4: The topology disambiguation diagram. The different color-coded regions delineate the range of values for  $R_2$  and  $P/E$  spanned by each decay topology from Fig. 2.

$M_A$ ,  $M_{\chi_1}$  and  $M_{\chi_2}$  can be simultaneously determined from a fit of eq. (18) to the data, just like in Fig. 3 [5].

*The topology of Fig. 2(d).* The invariant mass distribution of the visible particles  $v_1$  and  $v_2$  is not affected by the emission of invisible particles upstream and so this case is equivalent to the topology of Fig. 2(a). The corresponding results can be obtained from (5-9) with the substitution  $A \rightarrow B$ , since now the role of the parent resonance is played by the intermediate particle  $B$ . One would then be able to determine independently  $M_B$  and  $M_{\chi_2}$ , while  $M_A$  and  $M_{\chi_1}$  would remain unknown.

*The topology of Fig. 2(e).* Similarly, this case is equivalent to Fig. 2(b), with the substitutions  $A \rightarrow B_1$ ,  $B \rightarrow B_2$  and  $\chi \rightarrow \chi_2$ . Once again, the emission of the invisible particle  $\chi_1$  upstream is not observable. The only measurable parameter in this case will be the endpoint  $E$ .

*The topology of Fig. 2(f).* We find

$$\begin{aligned} f(m) &\sim m \int_{M_B^2(1 + \frac{m^2}{M_B^2 - M_{\chi_2}^2})}^{(M_A - M_{\chi_1})^2} \frac{ds}{s} \sqrt{\lambda(s, M_A^2, M_{\chi_1}^2)} \\ &\sim -m \left[ K_+ K_- + \ln \left( \frac{K_+ + K_-}{K_+ - K_-} \right)^{\frac{1}{2}(X_+^2 + X_-^2)} \right. \\ &\quad \left. + \ln \left( \frac{X_- K_+ - X_+ K_-}{X_- K_+ + X_+ K_-} \right)^{X_+ X_-} \right], \quad (20) \end{aligned}$$

where

$$X_\pm \equiv M_A \pm M_{\chi_1}, \quad K_\pm \equiv \sqrt{X_\pm^2 - K^2(m)}, \quad (21)$$

$$K^2(m) \equiv M_B^2 \left( 1 + \frac{m^2}{M_B^2 - M_{\chi_2}^2} \right), \quad (22)$$

$$E = \sqrt{((M_A - M_{\chi_1})^2 - M_B^2)(1 - M_{\chi_2}^2/M_B^2)}. \quad (23)$$

In this case, out of the 4 input masses entering the topology of Fig. 2(f), one can measure three independent degrees of freedom, e.g.  $M_A/M_B$ ,  $M_{\chi_1}/M_B$  and  $M_B^2 - M_{\chi_2}^2$ .

The topology of Fig. 2(g). The shape is described by

$$f(m) \sim m \int_{(M_{\chi_1} + M_{\chi_2})^2}^{M_B^2(1 - \frac{m^2}{M_A^2 - M_B^2})} \frac{ds}{s} \sqrt{\lambda(s, M_{\chi_1}^2, M_{\chi_1}^2)} \quad (24)$$

and it is easy to see that the results are obtained from (20-23) with the substitution  $M_A \leftrightarrow -M_{\chi_2}$ . In particular, the three measurable parameters in this case can be taken as  $M_{\chi_1}/M_B$ ,  $M_{\chi_2}/M_B$  and  $M_A^2 - M_B^2$ .

The topology of Fig. 2(h). This is the “sandwich” topology studied in [9]. The shape is given by

$$f(m) \sim \begin{cases} \eta m, & 0 \leq m \leq e^{-\eta} E, \\ m \ln(E/m), & e^{-\eta} E \leq m \leq E, \end{cases} \quad (25)$$

$$\eta \equiv \cosh^{-1} \left( \frac{M_{B_1}^2 + M_{B_2}^2 - M_{\chi_1}^2}{2M_{B_1}M_{B_2}} \right), \quad (26)$$

and

$$E = [e^{\eta}(M_A^2 - M_{B_1}^2)(M_{B_2}^2 - M_{\chi_2}^2)/(M_{B_1}M_{B_2})]^{1/2}, \quad (27)$$

$$P = \begin{cases} Ee^{-\eta}, & \eta < 1; \\ Ee^{-1}, & \eta \geq 1; \end{cases} \quad R_2 = \begin{cases} \infty, & \eta < 1; \\ 1, & \eta \geq 1. \end{cases} \quad (28)$$

The distribution (25) exhibits a cusp at the non-differentiable point  $m = e^{-\eta}E$ . In this case, there are 5 mass inputs:  $M_A$ ,  $M_{B_1}$ ,  $M_{B_2}$ ,  $M_{\chi_1}$  and  $M_{\chi_2}$ , but only two independent measurable parameters:  $\eta$  and  $E$ .

The topology of Fig. 2(i). This is the “antler” topology which was studied in [10] for the symmetric case of  $M_{B_1} = M_{B_2}$  and  $M_{\chi_1} = M_{\chi_2}$ . Here we generalize the result in [10] to arbitrary masses and find that  $f(m)$  is given by the same expression (25), only this time

$$\eta \equiv \cosh^{-1} \left( \frac{M_A^2 - M_{B_1}^2 - M_{B_2}^2}{2M_{B_1}M_{B_2}} \right), \quad (29)$$

$$E = [e^{\eta}(M_{B_1}^2 - M_{\chi_1}^2)(M_{B_2}^2 - M_{\chi_2}^2)/(M_{B_1}M_{B_2})]^{1/2} \quad (30)$$

and identical expressions (28) for  $P$  and  $R_2$ . Just like the case of Fig. 2(h), out of the 5 mass inputs,  $\eta$  and  $E$  are the only two measurable mass parameters. Table II

summarizes the final tally of input particle masses and independent measurable parameters for each topology.

Each topology from Fig. 2 also maps onto a restricted region in the  $(R_2, P/E)$  plane, as shown in Fig. 4 (for convenience, instead of  $R_2 \in (0, \infty)$ , in the figure we plot  $\frac{2}{\pi} \tan^{-1} R_2 \in (0, 1)$ ). For example, the cyan circle at (1, 1) marks the prediction for the two topologies of Fig. 2(b,e),

TABLE II: The number of mass inputs  $N_m$  for each topology in Fig. 2 and the number of independent measurable parameters  $N_p$  in the definition of  $f(m)$ .

Topology	(a,d)	(b,e)	(c)	(f,g)	(h,i)
$N_m$	2	3	3	4	5
$N_p$	2	1	3	3	2

while the magenta dot at (0.5, 0.37) and the magenta vertical line correspond to the two topologies of Fig. 2(h,i). The blue (red, green, black) points refer to the topologies of Fig. 2(a,d) (Fig. 2(g), Fig. 2(f), Fig. 2(c)). Fig. 4 demonstrates that with the three measurements  $E$ ,  $P$  and  $R_2$ , one can already begin to constrain qualitatively the allowed event topologies. A more quantitative comparison of the invariant mass shapes would have to employ a quantitative measure, such as the Kullback-Leibler distance [11]. Following [12], we revisit the antler topology example of Fig. 2(i) studied in [10]. Table III lists the number of events which are needed to disfavor the wrong event topologies by a factor of 1000. The table shows that, apart from the twin scenario of Fig. 2(h) which has the same invariant mass shape, all other alternatives will be ruled out with sufficient statistics.

TABLE III: The number of events needed to disfavor the wrong topology by a factor of 1000, if the data comes from the antler topology of Fig. 2(i) for the study point considered in [10]:  $M_A = 1500$  GeV,  $M_{B_1} = M_{B_2} = 730$  GeV and  $M_{\chi_1} = M_{\chi_2} = 100$  GeV.

Data	(a,d)	(b,e)	(c)	(f)	(g)	(h,i)
(i)	698	37	96	275	698	$\infty$

[1] A. Barr and C. Lester, J. Phys. G **37**, 123001 (2010).  
[2] Y. Bai and H. -C. Cheng, JHEP **1106**, 021 (2011).  
[3] E. Byckling and K. Kajantie, “Particle Kinematics”, John Wiley & Sons, 1973.  
[4] K. Agashe, D. Kim, D. G. E. Walker and L. Zhu, Phys. Rev. D **84**, 055020 (2011); G. F. Giudice, B. Gripaios and R. Mahbubani, Phys. Rev. D **85**, 075019 (2012).  
[5] W. Cho, D. Kim, K. Matchev and M. Park, to appear.  
[6] M. Blanke, D. Curtin and M. Perelstein, Phys. Rev. D **82**, 035020 (2010); A. Rajaraman and F. Yu, Phys. Lett. B **700**, 126 (2011); P. Baringer, K. Kong, M. McCaskey and D. Noonan, JHEP **1110**, 101 (2011).  
[7] I. Hinchliffe, F. Paige, M. Shapiro, J. Soderqvist and

W. Yao, Phys. Rev. D **55**, 5520 (1997); K. Matchev, F. Moortgat, L. Pape and M. Park, JHEP **0908**, 104 (2009).  
[8] W. S. Cho, K. Choi, Y. Kim and C. Park, Phys. Rev. Lett. **100**, 171801 (2008).  
[9] K. Agashe, D. Kim, M. Toharia and D. Walker, Phys. Rev. D **82**, 015007 (2010).  
[10] T. Han, I.-W. Kim and J. Song, Phys. Lett. B **693**, 575 (2010).  
[11] S. Kullback and R. Leibler, Ann. Math. Statist. **22**, 79 (1951).  
[12] C. Athanasiou, C. G. Lester, J. M. Smillie and B. R. Webber, JHEP **0608**, 055 (2006).